

## Article

# Rational Fabrication of Benzene-Linked Porous Polymers for Selective CO<sub>2</sub> Capture

Xiaofei Yan <sup>1,†</sup>, Fuqun Zhai <sup>1,†</sup>, Zifei Sun <sup>1</sup>, Jingwen Chen <sup>2</sup>, Dingming Xue <sup>1,\*</sup>  and Jie Miao <sup>3,\*</sup> 

<sup>1</sup> Nanjing Institute of Environmental Sciences, Ministry of Ecology and Environment, 8 Jiangwangmiao Street, Nanjing 210042, China

<sup>2</sup> Key Laboratory for Protected Agricultural Engineering in the Middle and Lower Reaches of Yangtze River, Institute of Agricultural Facilities and Equipment, Jiangsu Academy of Agricultural Sciences, Ministry of Agriculture and Rural Affairs, Nanjing 210014, China

<sup>3</sup> School of Environmental Science and Engineering, Nanjing Tech University, Nanjing 211816, China

\* Correspondence: xue\_dingming@nies.org (D.X.); miaojie@njtech.edu.cn (J.M.)

† These authors contributed equally to this work.

**Abstract:** Various porous polymer materials have been prepared for the separation of CO<sub>2</sub> from mixed gases. However, complex processes, expensive monomers, and costly catalysts are commonly used for their synthesis, making the adsorbents difficult to achieve in industrial applications. Herein, we developed a strategy to fabricate a series of benzene rings containing porous polymer materials (B-PPMs) via a facile condensation reaction of two inexpensive monomers, namely tetraphenylsilane and 1,4-bis(bromomethyl)benzene. The B-PPMs are verified to have accessible surface areas, large pore volumes, and appreciate pore sizes via a series of characterizations. The B-PPM-2 exhibits the best CO<sub>2</sub> adsorption amount of 67 cm<sup>3</sup>·g<sup>-1</sup> at 273 K and 1 bar, while the CO<sub>2</sub>/N<sub>2</sub> selectivity can reach 64.5 and 51.9 at 273 K and 298 K, respectively. Furthermore, the adsorbent B-PPM-2 can be completely regenerated after five cycles of breakthrough experiments under mild conditions, which may provide promising candidates for selective capture of CO<sub>2</sub> from mixtures.

**Keywords:** CO<sub>2</sub> capture; adsorption; selectivity; porous polymers; polymerization



**Citation:** Yan, X.; Zhai, F.; Sun, Z.; Chen, J.; Xue, D.; Miao, J. Rational Fabrication of Benzene-Linked Porous Polymers for Selective CO<sub>2</sub> Capture. *Separations* **2023**, *10*, 581. <https://doi.org/10.3390/separations10120581>

Academic Editor: Sohrab Zendehboudi

Received: 31 October 2023

Revised: 18 November 2023

Accepted: 21 November 2023

Published: 23 November 2023



**Copyright:** © 2023 by the authors. Licensee MDPI, Basel, Switzerland. This article is an open access article distributed under the terms and conditions of the Creative Commons Attribution (CC BY) license (<https://creativecommons.org/licenses/by/4.0/>).

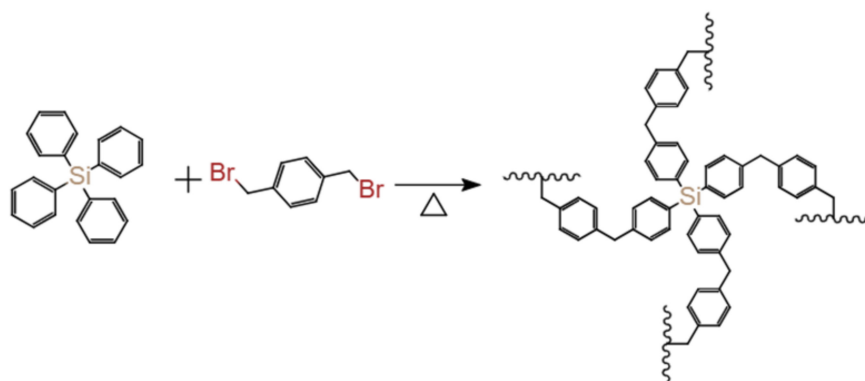
## 1. Introduction

Carbon dioxide, being a greenhouse gas, has wrought environmental havoc, severe pollution, weather calamities, and negative impacts on animals and plants and has become an urgent environmental crisis [1–3]. Carbon capture and storage is considered a presumable technology that can separate CO<sub>2</sub> from fossil fuels, thereby reducing the increasing carbon dioxide emissions into the atmosphere. Generally speaking, the traditional method for removing CO<sub>2</sub> is the ‘wet method’, namely chemical adsorption, which uses liquid ammonia solutions, such as monoethanolamine [4–6], diethanolamine [7,8], and diisopropanolamine [9,10]. However, solvent absorption methods have the disadvantages of severe equipment corrosion, high regeneration energy consumption, and decreased absorption capacity.

Different from the solvent adsorption process, the usage of solid adsorbents has the advantages of simple preparation, low cost, and environmental friendliness, which have been considered promising alternative methods for the effective removal of CO<sub>2</sub>. Up to now, a variety of porous materials, including metal oxides [11–13], mesoporous silica [14,15], activated carbon [16–19], porous organic polymers (POPs) [20–28], metal organic frameworks (MOFs) [29–31], and natural zeolites [32,33] has been prepared for the separation of CO<sub>2</sub> from mixed gases such as biogas and natural gas, showing enhanced capture performance. With widespread attention from the scientific and industrial communities, the design and preparation of adsorbent materials with higher adsorption capacity and lower costs have become the focus direction of solid adsorbent research at present.

According to the literature, MOFs exhibit excellent adsorption capacity for CO<sub>2</sub> because of their large specific surface area and high pore volume [34,35]. However, most reported MOFs are synthesized via complex processes and expensive monomers, and their structures are prone to collapse under high temperatures, moisture, and other harsh environments, rendering them unsuitable for industrial applications. As a porous solid adsorption material, POPs exhibit more stable physicochemical properties due to their stable covalent bond structure. For example, via condensation reactions of tris(4-aminophenyl)amine (TAPA) and 4,4',4''-boranetriyltris(2,3,5,6-tetramethylbenzaldehyde) (BTMA) with the presence of a catalyst, Zhai et al. synthesized the porous polymer, BTMA-TAPA-COF, which exhibited large surface areas of 630 m<sup>2</sup>·g<sup>-1</sup> and a good CO<sub>2</sub> capture capacity of 42 cm<sup>3</sup>·g<sup>-1</sup> [36]. Nevertheless, it should be stated that the BTMA was prepared from the dangerous and expensive monomer tert-Butyllithium at 195 K under a series of complex reactions. PAF-8 was synthesized via the Yamamoto-type Ullmann reactions from two monomers of tetraphenylsilane and formaldehyde dimethyl acetal without the presence of water and oxygen. The resultant PAF-8 possessed a high surface area of 785 m<sup>2</sup>·g<sup>-1</sup> as well as a good CO<sub>2</sub> capacity of 35.5 cm<sup>3</sup>·g<sup>-1</sup> [37]. Despite the numerous solid porous polymer materials that have been synthesized to date, the challenge remains in synthesizing the porous polymer materials from cost-effective monomers via a simple polymerization reaction with the absence of a catalyst.

In the present study, we devised and implemented a strategy to fabricate a series of benzene rings containing porous polymer materials (B-PPMs) via a straightforward condensation reaction involving tetraphenylsilane and 1,4-bis(bromomethyl)benzene (Scheme 1). The polymerization reactions can occur with the absence of any catalysts under mild conditions because of the proper reactivity of the reagent. In addition, the low-cost and readily available monomers without the use of the expensive catalyst enable a good economy and large-scale production of the B-PPMs in the future. The B-PPMs exhibit corresponding accessible surface areas and large pore volumes and appreciate pore sizes achieved by modulating the quantity of 1,4-bis(bromomethyl)benzene. The B-PPMs exhibit remarkable CO<sub>2</sub> capture performance, ranging from 38 to 67 cm<sup>3</sup>·g<sup>-1</sup> at 273 K and 1 bar. It is noteworthy that the B-PPM-2 displays outstanding CO<sub>2</sub> capture performance with a capacity of 67 cm<sup>3</sup>·g<sup>-1</sup>, which surpasses many other reported adsorbents, like BoxPOP-2 (34.7 cm<sup>3</sup>·g<sup>-1</sup>) [38], 476-MOF (47.6 cm<sup>3</sup>·g<sup>-1</sup>) [39], and A5 Zeolite (30.2 cm<sup>3</sup>·g<sup>-1</sup>) [32]. Additionally, the B-PPM-2 exhibits remarkable CO<sub>2</sub>/N<sub>2</sub> selectivity of 64.5 at 273 K and 0.1 bar. Notably, the B-PPM-2 also displays full regeneration performance without any significant decrease in capacity after six consecutive cycles. Furthermore, the adsorbent B-PPM-2 maintains strong separation performance after five cycles of breakthrough experiments, which may provide promising candidates for selective capture of CO<sub>2</sub> from CO<sub>2</sub>/N<sub>2</sub> mixtures.



**Scheme 1.** Synthetic route of the B-PPM-2.

## 2. Materials and Methods

### 2.1. Materials Synthesis

Commercial reagents of the tetraphenylsilane, 1,4-bis(bromomethyl)benzene, and tetrahydrofuran (THF) were purchased from Adamas-beta, Shanghai, China, and all the reagents were directly utilized without any further treatment. The ethanol and deionized water were employed for cleaning procedures during the preparation process of the adsorbents.

The minute synthesis route of the B-PPM-2 was drawn in Scheme 1. Then, 1 mmol tetraphenylsilane and 4 mmol 1,4-bis(bromomethyl)benzene were dissolved in the THF (50 mL) in turn. Then, the mixture solution was transferred to a sealed container and kept at constant temperature of 333 K for 48 h with continuous stirring. Upon cooling to room temperature, the filter cake was rinsed alternately with methanol and deionized water until the desired neutralization was achieved. With further vacuum drying overnight for the removal of the traces of methanol and moisture, the obtained residual was donated as B-PPM-2. All the B-PPMs were synthesized via the same reaction as drawn in Scheme 1. The resultant B-PPM-1, B-PPM-3, and B-PPM-4 are prepared successfully via the homologous synthesizing process, which corresponds to above-mentioned 1,4-bis(bromomethyl)benzene reaction molar amount of 8 mmol, 2 mmol, and 1 mmol, respectively.

### 2.2. Characterization

The fracture and generation of chemical bonds are direct evidence for detecting the successful preparation of materials. Fourier transform infrared (FTIR) spectra of the samples were recorded on a Nicolet Nexus 360 spectrometer (Thermo Nicolet, Waltham, USA). The flakes were uniformly mixed using the adsorbent and potassium bromide in a mass ratio of 1:150 and tested for 32 scans with a wavenumber between  $4000\text{ cm}^{-1}$  and  $650\text{ cm}^{-1}$ . The X-ray powder diffraction (XRPD) patterns could characterize crystal structure of the B-PPMs and were recorded using the Bruker D8 Advance diffractometer (Bruker, Billerica, USA). The detailed experiment conditions included the  $2\theta$  range of 5–60, the step size of  $0.02^\circ$ , and the scan rate of  $1^\circ\cdot\text{min}^{-1}$ . Thermogravimetry (TG) analyses were performed with a TGA209F3 (Netzsch, Bavaria, Germany) apparatus to obtain thermal stability. The B-PPMs were heated from 298 K to 1073 K at a heating rate of  $10\text{ K}\cdot\text{min}^{-1}$ , with the protective atmosphere of high-purity nitrogen (99.999%) avoiding oxidation. Images of high-resolution transmission electron microscopy (HRTEM) were obtained using a JEM-2010 UHR electron microscope (JEOL, Tokyo, Japan). The scanning electron microscope (SEM) images were observed on a Hitachi S-4800 (Hitachi, Tokyo, Japan). The  $\text{N}_2$  adsorption–desorption isotherms were conducted to explore the structural properties of the B-PPMs at 77 K with BSD-660 (BSD, Beijing, China). Prior to the isotherm test, the B-PPMs were dried at 383 K under vacuum conditions for 1 h. The samples of 0.1 g were heated in a vacuum-drying oven for 3 h and then quickly transferred to the analyzer tube to prevent contamination from moisture and impurities in the air.

### 2.3. Adsorption Tests

The ASAP 2020 analyzer (Micromeritics, Atlanta, GA, USA) was employed for the  $\text{CO}_2$ ,  $\text{CH}_4$ , and  $\text{N}_2$  (pure, 99.999%) static adsorption over the B-PPMs at 273 K and 298 K and 0–1 bar. The helium was used to measure the dead volume due to the fact that helium was rarely adsorbed into the B-PPMs. The isosteric heats of adsorption ( $Q_{st}$ ) were employed to illustrate the interaction between the B-PPMs and the gas molecules and calculated using the Clausius–Clapeyron equation. To predict the selectivity of  $\text{CO}_2$  over  $\text{N}_2$  and  $\text{CH}_4$ , the ideal adsorption solution theory (IAST) was employed. The IAST was defined as  $(x_i/y_i)/(x_j/y_j)$ , in which  $x_i$  and  $y_i$  ( $x_j$  and  $y_j$ ) were the molar fractions of component 1 (component 2) in the adsorbed and bulk phases, respectively.

Dynamic breakthrough experiments were critical to further probe the potential of B-PPM-2 in industrial production. Approximately 0.5 g B-PPM-2 were filled into a special glass tube and dried under vacuum for 1 h at 393 K, then submerged in the mixture of

ice and water. The CO<sub>2</sub>/N<sub>2</sub> (15/85, *v/v*) mixture was fed into the system at the rate of 3 mL·min<sup>-1</sup> at 273 K and 1 bar. The composition of each component gas at the outlet was precisely recorded every 30 s using automated gas chromatography and drawn as the dynamic breakthrough curves.

### 3. Results and Discussion

#### 3.1. Characterization

The FT-IR spectra and TG curves of the B-PPMs are listed in Figure 1a and 1b, respectively. The B-PPMs' successful fabrication can be confirmed via the FT-IR spectra, which are listed in Figure 1a. The -C-Si- bond of the reagent tetraphenylsilane is readily recognized by its stretching vibration bands, which are located at 736 cm<sup>-1</sup> and 803 cm<sup>-1</sup> [40,41]. These two stretching vibration peaks of -C-Si- are observable in the B-PPMs, illustrating the successful introduction of tetraphenylsilane to the B-PPMs. The intense stretching vibration of -C-Br- of the monomer 1,4-bis(bromomethyl)benzene located at 743 cm<sup>-1</sup> is weakened in the B-PPMs, exhibiting the break of the -C-Br- during the fabrication process. These results imply the B-PPMs are successfully fabricated via a facile condensation reaction.

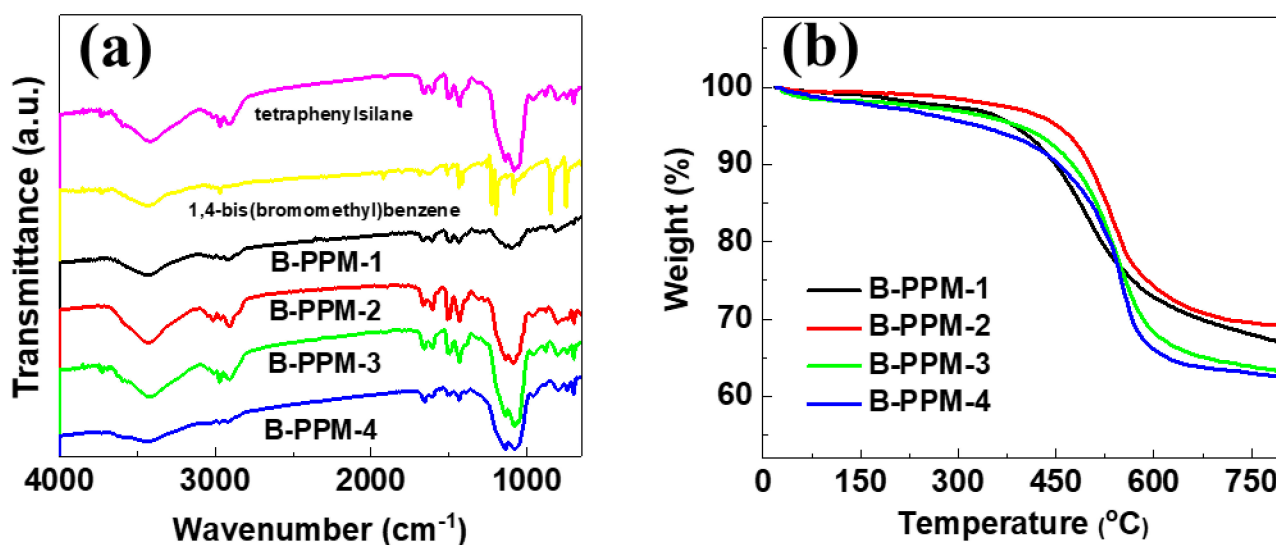


Figure 1. (a) FT-IR spectra and (b) TG curves of the B-PPMs.

Figure 1b shows the TG curves of the B-PPMs, which reflect the thermal stability information. All the samples show two main weight loss processes, and the adsorbed trace water and impurities quickly escape from the pore structure of the B-PPMs at around 150 °C. A sharp weight loss appears, ranging from 450 °C to 600 °C, giving evidence of the high thermal stability of the B-PPMs. It is obviously observed that the B-PPM-2 shows a high initial decomposition temperature of about 450 °C, which is higher than that of B-PPM-1 as well as that of B-PPM-3 and B-PPM-4. Remarkably, the B-PPM-2 manifests a total weight residual of 69%, which is bigger in contrast to that of the B-PPM-1, B-PPM-3, and B-PPM-4 (correspond to 66%, 63%, and 62%, respectively). The difference in the thermal stability is dictated by introducing 1,4-bis(bromomethyl)benzene. The high-quality residue remaining after the heat treatment indicates the successful synthesization of the B-PPMs with a high crosslinking degree from the two simple reactants. The amorphous characteristics of the B-PPMs are validated via the XRD in Figure S1, and no intense diffraction peaks are observed [42].

All four N<sub>2</sub> adsorption-desorption isotherms of the B-PPMs are drawn in Figure 2a and the corresponding pore size distribution of the B-PPMs are drawn in Figure 2b. It is obvious that the isotherms of the B-PPMs are assigned to the characteristic IV-type isotherm. At the relative pressure ranging from 0 to 0.05, the B-PPMs exhibit a linear increase in the amount

of captured N<sub>2</sub>, which is relevant to the high porosity. With the relative pressure increase of more than 0.1, the B-PPMs still illustrate a rapid escalation in N<sub>2</sub> uptakes along with visible hysteresis loops. These results indicate that the B-PPMs achieve a great deal of micropores and mesopores, which results from the condensation reaction of the two monomers. As the introducing amount of the monomer 1,4-bis(bromomethyl)benzene decreases, the B-PPMs show a marked decline in N<sub>2</sub> uptakes. It is believed that the 1,4-bis(bromomethyl)benzene significantly determines the pore structure of the B-PPMs.

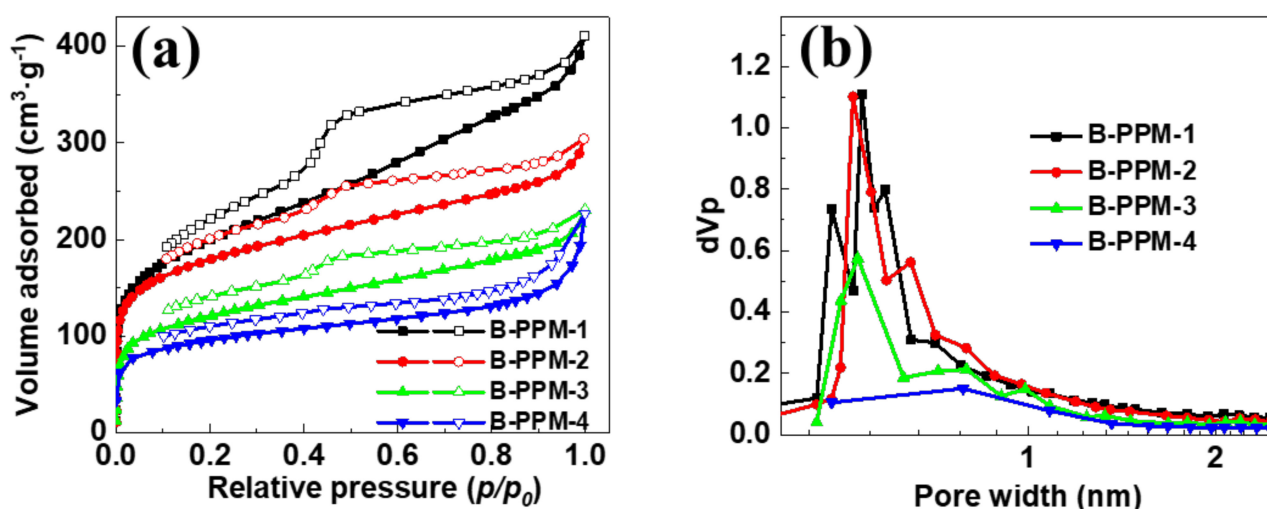


Figure 2. (a) Nitrogen adsorption–desorption isotherms at 77 K; (b) corresponding pore size distributions of B-PPMs.

As listed in Table 1, the calculated specific surface areas of the B-PPMs have been calculated upon the N<sub>2</sub> adsorption–desorption isotherms. The B-PPM-1 owns the largest surface area, meaning 680 m<sup>2</sup>·g<sup>-1</sup>, surpassing the B-PPM-2, B-PPM-3, and B-PPM-4, which registered surface areas of 593 m<sup>2</sup>·g<sup>-1</sup>, 405 m<sup>2</sup>·g<sup>-1</sup>, and 309 m<sup>2</sup>·g<sup>-1</sup>, respectively. In line with the tendency of the specific surface area, the B-PPM-1 possesses the highest total pore volume of 0.61 cm<sup>3</sup>·g<sup>-1</sup>, while the total pore volume of the B-PPM-2, B-PPM-3, and B-PPM-4 range from 0.49 cm<sup>3</sup>·g<sup>-1</sup> to 0.26 cm<sup>3</sup>·g<sup>-1</sup>.

Table 1. Porosity properties of B-PPMs.

Sample	S <sub>BET</sub> (m <sup>2</sup> ·g <sup>-1</sup> )	V <sub>total</sub> (cm <sup>3</sup> ·g <sup>-1</sup> )	V <sub>meso</sub> (cm <sup>3</sup> ·g <sup>-1</sup> )	V <sub>micro</sub> (cm <sup>3</sup> ·g <sup>-1</sup> )
B-PPM-1	680	0.61	0.33	0.28
B-PPM-2	593	0.49	0.24	0.25
B-PPM-3	405	0.34	0.20	0.14
B-PPM-4	309	0.26	0.17	0.09

As shown in Figure 2b, the corresponding pore size distribution of the B-PPMs illustrates that all the B-PPMs possess abundant micropores, which are favorable for the CO<sub>2</sub> molecules immobilization. The B-PPM-1 exposes the ultra-micropores between 0.45 nm to 0.81 nm. Simultaneously, the B-PPM-2 exhibits micropores around 0.52–0.83 nm, slightly less than those observed in B-PPM-1, a consequence of the decreased introduction of the 1,4-bis(bromomethyl)benzene. With decreasing the 1,4-bis(bromomethyl)benzene content, the pore structures of the polymer-PPMs are undeveloped evidently, as previously mentioned. The B-PPM-3 and B-PPM-4 both show fewer pores, which are located around between 0.45 and 0.85 nm and between 0.55 and 0.9 nm, respectively. In accordance with the TG curves, these results indicate that the 1,4-bis(bromomethyl)benzene determines the pore structures of the porous polymer. It is clearly observed that all the B-PPMs mainly

reveal microporous structures. Based on previous work, the micropores are regarded as responsible for gas storage and transport [43–45]. Consequently, the synthesized B-PPMs with large surface areas and well-distributed micropores possess great potential for use in gas separation and storage.

The surface morphologies and pore structures of the B-PPMs are observed using SEM. As shown in Figure S2, all of the B-PPMs exhibit irregular block morphology with disordered channels and pores. The TEM images of the representative sample B-PPM-2 are displayed in Figure S3, and the images highlight the abundant micropores with the wormhole-like arrangement of B-PPM-2 from macropores to micropores that are hyperconnected.

### 3.2. Gas Adsorption Performance

The gas capture performance of adsorbents B-PPMs for pure single-component CO<sub>2</sub> was investigated and shown in Figure 3a, while Figure 3b,c exhibit the CO<sub>2</sub> isosteric heat of the B-PPMs and the IAST selectivity for the B-PPM-2. With the absolute pressure increased from 0 to 1 bar, all the B-PPMs emerge a tendency for the CO<sub>2</sub> amount to increase steadily and gently at 273 K. These adsorption isotherms indicate the reality that the accessible pore structures of the B-PPMs have been occupied by a great deal of CO<sub>2</sub> molecules. For instance, B-PPM-1 demonstrates a CO<sub>2</sub> adsorption capacity of 52 cm<sup>3</sup>·g<sup>-1</sup>, primarily attributed to its high surface area of 680 m<sup>2</sup>·g<sup>-1</sup> and total pore volume of 0.61 cm<sup>3</sup>·g<sup>-1</sup>. As reported in the literature, a higher specific surface area of the adsorbent always supplies the more available accessible pores and achieves the higher CO<sub>2</sub> adsorption capacity [44,46,47]. Consequently, it is beyond question that the insufficient pore structure of the B-PPM-3 and B-PPM-4, characterized by smaller surface area (405 m<sup>2</sup>·g<sup>-1</sup> and 309 m<sup>2</sup>·g<sup>-1</sup>) and pore volume (0.34 cm<sup>3</sup>·g<sup>-1</sup> and 0.26 cm<sup>3</sup>·g<sup>-1</sup>), lead to the lower CO<sub>2</sub> uptake of 41 cm<sup>3</sup>·g<sup>-1</sup> and 38 cm<sup>3</sup>·g<sup>-1</sup>.

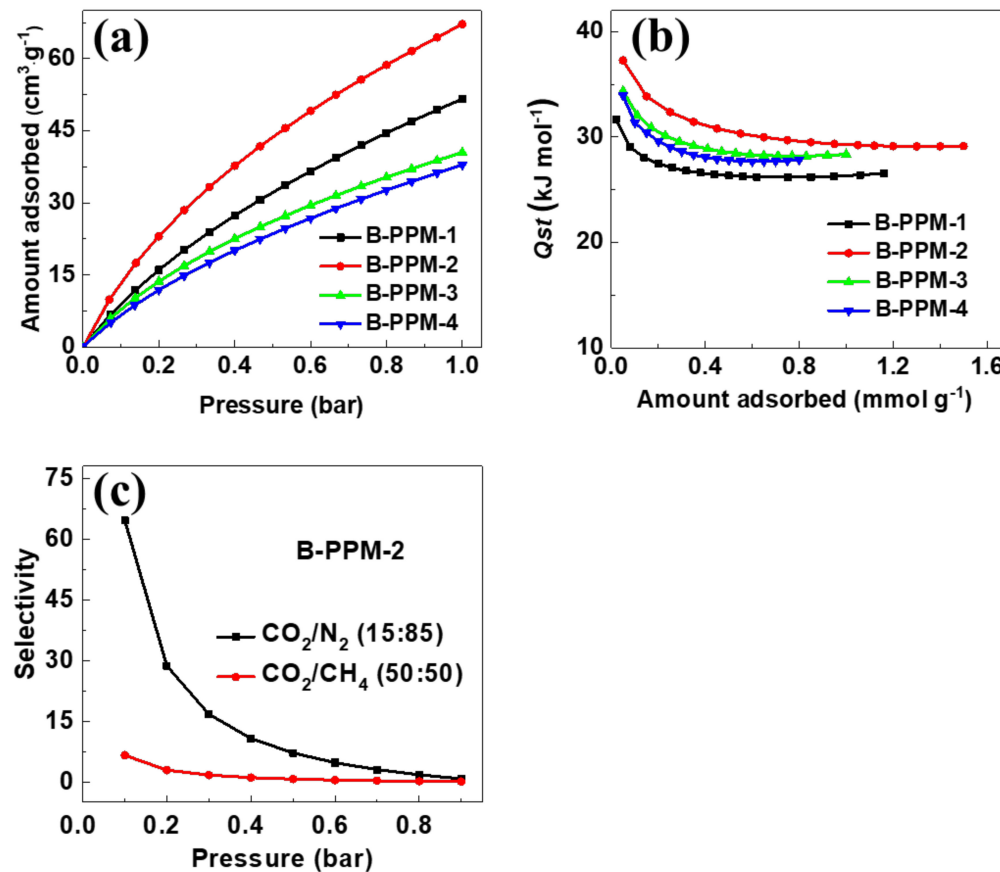


Figure 3. (a) CO<sub>2</sub> adsorption isotherms of the B-PPMs at 273 K, (b) CO<sub>2</sub> isosteric heat of adsorption of the B-PPMs, (c) IAST selectivity of CO<sub>2</sub>/N<sub>2</sub> (15:85) and CO<sub>2</sub>/CH<sub>4</sub> (50:50) on the B-PPM-2 at 273 K.

However, the largest surface area does not have responsibility for ensuring the highest CO<sub>2</sub> adsorptive capacity, and the B-PPM-2 demonstrate the highest CO<sub>2</sub> adsorptive capacity of 67 cm<sup>3</sup>·g<sup>-1</sup>, which is also better than much other literature data (as listed in Table 2), such as 476-MOF (47.6 cm<sup>3</sup>·g<sup>-1</sup>) [39], BoxPOP-2 (34.7 cm<sup>3</sup>·g<sup>-1</sup>) [38], 13X-PEI-60 (48.2 cm<sup>3</sup>·g<sup>-1</sup>) [48], A5 Zeolite (30.2 cm<sup>3</sup>·g<sup>-1</sup>) [32], and P2 (67.6 cm<sup>3</sup>·g<sup>-1</sup>) [49]. Even more interesting is that the B-PPM-2 possesses a lower surface area (593 m<sup>2</sup>·g<sup>-1</sup>) and pore volume (0.34 cm<sup>3</sup>·g<sup>-1</sup>) compared with the B-PPM-1. This contrastive result confirms that the surface area is not the sole determinant of CO<sub>2</sub> adsorptive capacity. The pore size of B-PPMs is also beneficial to the improvement of the CO<sub>2</sub> adsorptive performance. As previous work reported, theoretical calculation indicates that Van der Waal's interaction between the captured CO<sub>2</sub> and the pores of the adsorbents generates powerful heat effects. Along with the reduction in the pore diameters from 2 nm to 0.5 nm, the calculated adsorption heat values range from 18.9 kJ·mol<sup>-1</sup> to 29.6 kJ·mol<sup>-1</sup> [50]. Similar results are shown in Figure 3b: all the *Q<sub>st</sub>* values of the B-PPMs are located around the 26 kJ·mol<sup>-1</sup> to 37 kJ·mol<sup>-1</sup>, exhibiting that the *Q<sub>st</sub>* results from the CO<sub>2</sub> capacity into the micropore structure of the B-PPMs. It is interesting that the *Q<sub>st</sub>* value of the B-PPM-2 is always slightly bigger than that of the B-PPM-1, B-PPM-3, and B-PPM-4 at a certain adsorption capacity, Originating from the more developed micropore structure of the B-PPM-2. When the pore diameter falls below 0.5 nm, the so-called ultra-micropores are rendered useless because the CO<sub>2</sub> molecules are prevented from accessing the tiny space [50]. In the case of the B-PPM-1, the micropores with sizes less than 0.5 nm do not help in capturing the CO<sub>2</sub> molecular, while the B-PPM-2 is instrumental in immobilizing the CO<sub>2</sub> molecular because of the micropore size about 0.52–0.83 nm. Therefore, the efficient improvement of the CO<sub>2</sub> adsorptive capacity originates from the synergistic effect of the specific surface area, pore volume, and appropriate micropore size of the B-PPMs.

**Table 2.** The adsorption capacity and selectivity for the different adsorbents.

Samples	T/K	S <sub>BET</sub> (m <sup>2</sup> ·g <sup>-1</sup> )	CO <sub>2</sub> Uptake <sup>a</sup> (cm <sup>3</sup> ·g <sup>-1</sup> )	Selectivity <sup>b</sup> CO <sub>2</sub> /N <sub>2</sub>	Ref.
B-PPM-2	273	593	67	64.5	This work
A5 Zeolite	273	179	30.2	NA	[32]
BoxPOP-2	273	225	34.7	NA	[38]
476-MOF	273	898	47.6	75	[39]
CAGE	298	32	23	40	[42]
M90_0.5	298	328	47	53	[51]
13X-PEI-60	273	1.3	48.2	NA	[48]
PEI-100CP-MAG	348	NA	11.2	110	[52]
P2	273	242	67.6	34	[49]
TPI-5	273	201	35	46	[25]
CO <sub>2</sub> -NPC-800-15	273	34.9	20.2	NA	[53]
AHEP	273	418	31	47	[54]

<sup>a</sup> The CO<sub>2</sub> uptake is tested at 1 bar. <sup>b</sup> The selectivity of CO<sub>2</sub>/N<sub>2</sub> are calculated at 0.1 bar. NA, not available.

As shown in Figure S4, the adsorption isotherms of CO<sub>2</sub>, CH<sub>4</sub>, and N<sub>2</sub> on B-PPMs are systematically investigated. Under the influence of a higher temperature of 298 K at 1 bar, the CO<sub>2</sub> uptakes of the B-PPMs manifest a marked decline. For example, the adsorption capacity of B-PPM-2 has decreased from 67 cm<sup>3</sup>·g<sup>-1</sup> to 34 cm<sup>3</sup>·g<sup>-1</sup>. All four B-PPM polymers show reasonable CO<sub>2</sub> adsorptive capacity and barely a few N<sub>2</sub> uptakes. The sample B-PPM-2 not only exhibits the best adsorption performance for CO<sub>2</sub> but also has the highest adsorption capacity for CH<sub>4</sub> (18 cm<sup>3</sup>·g<sup>-1</sup>) and N<sub>2</sub> (3 cm<sup>3</sup>·g<sup>-1</sup>) at 273 K and 1 bar, signifying that the B-PPM-2 has a latent capacity for industrial applications, particularly in the separation of the CO<sub>2</sub>/N<sub>2</sub> and CO<sub>2</sub>/CH<sub>4</sub> gas mixture. The selectivity of CO<sub>2</sub>/CH<sub>4</sub> and CO<sub>2</sub>/N<sub>2</sub> for the B-PPM-2 at 273 K and 298 K were determined using the IAST model, as depicted in Figure 3c and Figure S5. Wherein, the mixture gases have a resemblance with the typical industrial gas composition, with the CO<sub>2</sub>/CH<sub>4</sub> and CO<sub>2</sub>/N<sub>2</sub> ratios of 50/50

and 15/85. At 273 K and 0.1 bar, the  $\text{CO}_2/\text{N}_2$  selectivity of the B-PPM-2 is as high as 64.5, making allowances for the relatively few captured amounts of  $\text{N}_2$ . The selectivity value of 64.5 for the B-PPM-2 is higher than much other literature data (as listed in Table 2, e.g., 40 for CAGE [42], 53 for M90\_0.5 [51], 34 for P2 [49], 46 for TPI-5 [25], and 47 for AHEP [54]). Compared with some membranes reported in the literature, such as 64 for PPS/PSf (298 K, 5 bar) [55] and 54.8 for Cu-BTC-SC/Pebax (298 K, 1.5 bar) [56], the B-PPM-2 are equally capable of selectively separating the  $\text{CO}_2$  from the mixture. The  $\text{CO}_2/\text{CH}_4$  selectivity of the B-PPM-2 is 6.6 at 273 K and 0.1 bar, which slightly decreases to 5.1 upon the high temperature. Moreover, the IAST selectivity on the B-PPM-2 sample at 273 K and a certain pressure are invariably higher than those at 298 K. For example, at the 0.3 bar, the  $\text{CO}_2/\text{N}_2$  selectivity on B-PPM-2 is 16.7 at 273 K, which is higher than 13.4 at 298 K. The results indicate that the B-PPM-2 can produce a marked effect on  $\text{CO}_2$  purification in the  $\text{CO}_2/\text{CH}_4$  and  $\text{CO}_2/\text{N}_2$  mixed systems.

In general, the sorbent regeneration stage is the most critical step of  $\text{CO}_2$  capture. Numerous regeneration methods have been used in the different regeneration strategies (e.g., PSA, TSA, and VSA) [57,58]. In this case, the method of regeneration in situ is accepted since the porous materials B-PPMs are prepared and tested in the lab. To further investigate the feasibility of the long-term use of the industrial separation of B-PPM-2, consecutive recycling experiments were conducted, as shown in Figure 4a. The adsorption/desorption isotherms of  $\text{CO}_2$  for the B-PPM-2 were measured for six cycles. It is clear that there is a slight loss of  $\text{CO}_2$  adsorption capacity during the continuous six cycles. In a single cycle, the adsorption isotherm exhibits a smooth increase, and the desorption isotherm shows the absolute removal of the adsorbed  $\text{CO}_2$  gases. Following the completion of the entire adsorption/desorption process, a very mild vacuum step is operated at 273 K and maintained for 1 h. After the six cycles, all the adsorption/desorption isotherms are almost coincident, indicating the excellent  $\text{CO}_2$  adsorption regeneration of the B-PPM-2. Compared with the initial  $\text{CO}_2$  adsorptive capacity of  $67 \text{ cm}^3 \cdot \text{g}^{-1}$ , the adsorptive capacity for the sixth cycle is approximately  $66.2 \text{ cm}^3 \cdot \text{g}^{-1}$ , indicating nearly equivalent performance. These results demonstrate that by only adjusting the operating pressure,  $\text{CO}_2$  can be entirely released without any residue from the samples. The excellent regeneration will give the B-PPM-2 a passport to the application in the pressure swing adsorption technology (PSA).

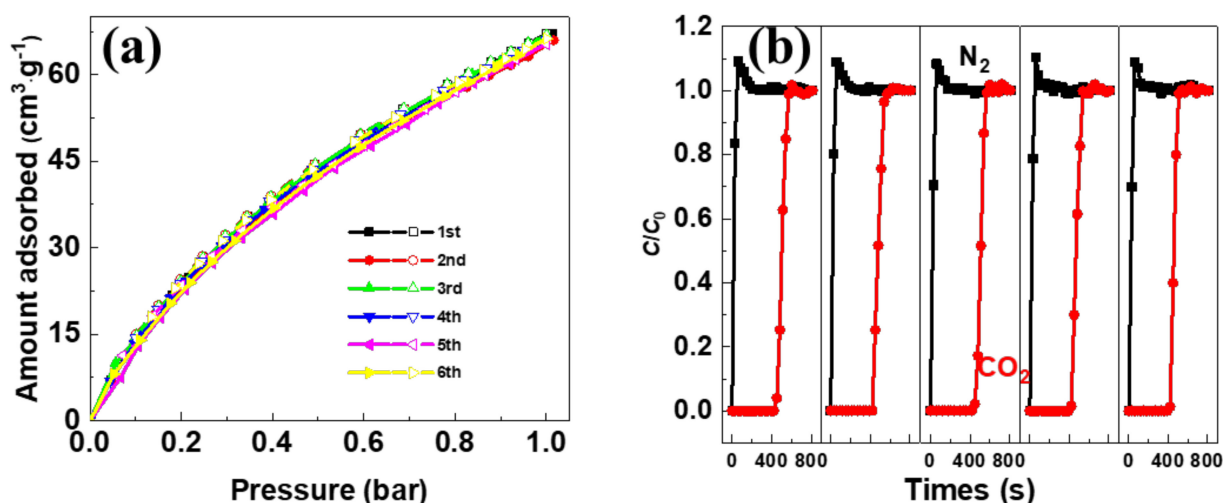


**Figure 4.** (a) Six adsorption/desorption cycles of  $\text{CO}_2$  over B-PPM-2 at 273 K and 1 bar. (b) Dynamic breakthrough curves of the B-PPM-2 for  $\text{CO}_2/\text{N}_2$  mixture.

Moreover, the price of the porous adsorbents is a crucial factor for the sustained use of industrial separation. The gas separation process over the various solid adsorbents is inherently similar. Therefore, the costs of the monomers and the catalysis mainly determine the overall cost of porous adsorbents. A comparison of the cost of adsorbents based on

the price of monomers and catalysts is listed in Table S1. It is important to note that the calculated price of the adsorbents is based on a rough estimation under realistic reaction conditions. Numerous additional factors, such as reaction temperature, duration, multi-level reactions, and pressure, may impact product prices but are not fully considered in this analysis. Consequently, in view of these data, it is evident that the rough price of our material B-PPM-2 is less than that of some reported porous adsorbents.

Dynamic breakthrough experiments are important to further assess the selective adsorption performance of B-PPM-2 in the PSA. As depicted in Figure 4b, in the case of the first dynamic breakthrough experiment for the B-PPM-2, N<sub>2</sub> is the first component to break via the fixed bed. This observation is attributed to the poor capture of N<sub>2</sub> via B-PPM-2. Moreover, the CO<sub>2</sub> breaks the fixed bed over B-PPM-2 at 450 s, which is much longer than 30 s of N<sub>2</sub>. In the case of the fifth dynamic breakthrough experiment, the N<sub>2</sub> molecular escape from the fixed bed as quickly as around 30 s is out of the question. Correspondingly, the CO<sub>2</sub> breaks the fixed bed over B-PPM-2 at 420 s, which is a slight fluctuation, compared with the 450 s of the initial one. These results of the dynamic breakthrough curve of the B-PPM-2 are consistent with the single-component adsorption isotherms, indicating more powerful evidence for the potential application over high-efficient CO<sub>2</sub> capture from gas mixtures. Altogether, the excellent recycling performance and low price further confirm that our porous material B-PPM-2 is a promising adsorbent for the separation of CO<sub>2</sub>/N<sub>2</sub>.

#### 4. Conclusions

In this work, a series of porous polymer B-PPMs originated from the facile polymerization of the tetraphenylsilane and 1,4-bis(bromomethyl)benzene were synthesized successfully. The introduction amount variation of the 1,4-bis(bromomethyl)benzene monomer is important to upgrade the pore structure of the B-PPMs. The B-PPM-2, distinguished by the substantial surface area, generous pore volume, and well-suited micropore size, not only effectuates an outstanding CO<sub>2</sub> capture capacity of 67 cm<sup>3</sup>·g<sup>-1</sup> but also displays a remarkable CO<sub>2</sub>/N<sub>2</sub> selectivity of 64.5. We believe that our B-PPMs have potential as competitive candidates for CO<sub>2</sub> adsorbents, and this facile synthetic protocol can be further developed to achieve superior porous polymer materials.

**Supplementary Materials:** The following supporting information can be downloaded at: <https://www.mdpi.com/article/10.3390/separations10120581/s1>, Figure S1: XRD pattern of the B-PPMs. Figure S2: SEM images of the (a) B-PPM-1, (b) B-PPM-2, (c) B-PPM-3 and (d) B-PPM-4. Figure S3: TEM images (a) 100 nm and (b) 10 nm of the B-PPM-2. Figure S4: CO<sub>2</sub>, N<sub>2</sub>, and CH<sub>4</sub> adsorption isotherms of the sample (a) B-PPM-1, (b) B-PPM-2, (c) B-PPM-3, and (d) B-PPM-4 at 273 K and 298 K and 1 bar. Figure S5: IAST selectivity of CO<sub>2</sub>/N<sub>2</sub> (15:85) and CO<sub>2</sub>/CH<sub>4</sub> (50:50) on the B-PPM-2 at 298 K.

**Author Contributions:** Conceptualization, D.X. and J.M.; methodology, X.Y., F.Z., and Z.S.; software, X.Y., F.Z., and J.C.; validation, D.X. and J.M.; writing—original draft preparation, X.Y. and F.Z.; writing—review and editing, D.X. and J.M.; funding acquisition, J.M. All authors have read and agreed to the published version of the manuscript.

**Funding:** This work was supported by the National Natural Science Foundation of China (No. 22106104 and No. 22308293), Natural Science Foundation of Shandong Province (No. ZR2020QB176), and Jiangsu Agricultural Science and Technology Innovation Fund (No. CX(23)3111).

**Data Availability Statement:** Data are contained within this article or Supplementary Material.

**Conflicts of Interest:** The authors declare no conflict of interest.

#### References

1. Song, K.S.; Fritz, P.W.; Coskun, A. Porous organic polymers for CO<sub>2</sub> capture, separation and conversion. *Chem. Soc. Rev.* **2022**, *51*, 9831–9852. [[CrossRef](#)] [[PubMed](#)]
2. Ozkan, M.; Nayak, S.P.; Ruiz, A.D.; Jiang, W. Current status and pillars of direct air capture technologies. *iScience* **2022**, *25*, 103990. [[CrossRef](#)] [[PubMed](#)]

3. De Kleijne, K.; Hanssen, S.V.; van Dinteren, L.; Huijbregts, M.A.J.; van Zelm, R.; de Coninck, H. Limits to Paris compatibility of CO<sub>2</sub> capture and utilization. *One Earth* **2022**, *5*, 168–185. [[CrossRef](#)]
4. Xie, F.; Sun, W.; Pinacho, P.; Schnell, M. CO<sub>2</sub> aggregation on monoethanolamine: Observations from rotational spectroscopy. *Angew. Chem. Int. Ed.* **2023**, *62*, e202218539. [[CrossRef](#)] [[PubMed](#)]
5. Jørsboe, J.K.; Vinjarapu, S.H.B.; Neerup, R.; Møller, A.C.; Jensen, S.; Abildskov, J.; Fosbøl, P. Mobile pilot plant for CO<sub>2</sub> capture in biogas upgrading using 30 wt% MEA. *Fuel* **2023**, *350*, 128702–128713. [[CrossRef](#)]
6. Zhou, Y.; Li, P.; Wang, Y.; Zhao, Q.; Sun, H. Progress in the separation and purification of carbon hydrocarbon compounds using MOFs and molecular sieves. *Separations* **2023**, *10*, 543. [[CrossRef](#)]
7. Ghalib, L.; Abdulkareem, A.; Ali, B.S.; Mazari, S.A. Modeling the rate of corrosion of carbon steel using activated diethanolamine solutions for CO<sub>2</sub> absorption. *Chin. J. Chem. Eng.* **2020**, *28*, 2099–2110. [[CrossRef](#)]
8. Rashidi, H.; Sahraie, S. Enhancing carbon dioxide absorption performance using the hybrid solvent: Diethanolamine-methanol. *Energy* **2021**, *221*, 119799. [[CrossRef](#)]
9. Choi, B.-K.; Kim, S.-M.; Kim, K.-M.; Lee, U.; Choi, J.H.; Lee, J.-S.; Baek, I.H.; Nam, S.C.; Moon, J.-H. Amine blending optimization for maximizing CO<sub>2</sub> absorption capacity in a diisopropanolamine–methyldiethanolamine–H<sub>2</sub>O system using the electrolyte UNIQUAC model. *Chem. Eng. J.* **2021**, *419*, 129517. [[CrossRef](#)]
10. Haghtalab, A.; Gholami, V. Carbon dioxide solubility in the aqueous mixtures of diisopropanolamine + l-arginine and diethanolamine + l-arginine at high pressures. *J. Mol. Liq.* **2019**, *288*, 111064. [[CrossRef](#)]
11. Seah, G.L.; Wang, L.; Tan, L.F.; Tipjanrawee, C.; Sasangka, W.A.; Usadi, A.K.; McConnachie, J.M.; Tan, K.W. Ordered mesoporous alumina with tunable morphologies and pore sizes for CO<sub>2</sub> capture and dye separation. *ACS Appl. Mater. Interfaces* **2021**, *13*, 36117–36129. [[CrossRef](#)] [[PubMed](#)]
12. Kwon, S.; Yang, H.; Yu, Y.; Choi, Y.; Kim, N.; Kim, G.H.; Ko, K.C.; Na, K. A sustainable carbon-consuming cycle based on sequential activation of CO<sub>2</sub> and CH<sub>4</sub> using metal oxides. *Appl. Catal. B Environ.* **2023**, *339*, 123120. [[CrossRef](#)]
13. Mat, N.; Timmiati, S.N.; Teh, L.P. Recent development in metal oxide-based core-shell material for CO<sub>2</sub> capture and utilisation. *Appl. Nanosci.* **2022**, *13*, 3797–3817. [[CrossRef](#)]
14. Wang, H.; Liu, X.; Saliy, O.; Hu, W.; Wang, J. Robust amino-functionalized mesoporous silica hollow spheres templated by CO<sub>2</sub> bubbles. *Molecules* **2021**, *27*, 53. [[CrossRef](#)] [[PubMed](#)]
15. Wang, Y.; Huang, L.; Li, S.; Liu, C.; He, H. The capture and catalytic conversion of CO<sub>2</sub> by dendritic mesoporous silica-based nanoparticles. *Energy Environ. Mater.* **2023**, *6*, e12593. [[CrossRef](#)]
16. Pardakhti, M.; Jafari, T.; Tobin, Z.; Dutta, B.; Moharrer, E.; Shemshaki, N.S.; Suib, S.; Srivastava, R. Trends in solid adsorbent materials development for CO<sub>2</sub> capture. *ACS Appl. Mater. Interfaces* **2019**, *11*, 34533–34559. [[CrossRef](#)] [[PubMed](#)]
17. Wang, J.; Senkovska, I.; Oschatz, M.; Lohe, M.R.; Borchardt, L.; Heerwig, A.; Liu, Q.; Kaskel, S. Imine-linked polymer-derived nitrogen-doped microporous carbons with excellent CO<sub>2</sub> capture properties. *ACS Appl. Mater. Interfaces* **2013**, *5*, 3160–3167. [[CrossRef](#)]
18. Li, P.; Xing, C.; Qu, S.; Li, B.; Shen, W. Carbon dioxide capturing by nitrogen-doping microporous carbon. *ACS Sustain. Chem. Eng.* **2015**, *3*, 1434–1442. [[CrossRef](#)]
19. Melke, J.; Schuster, R.; Möbus, S.; Jurzinsky, T.; Elsässer, P.; Heilemann, A.; Fischer, A. Electrochemical stability of silica templated polyaniline derived mesoporous N-doped carbons for the design of Pt based oxygen reduction reaction catalysts. *Carbon* **2019**, *146*, 44–59. [[CrossRef](#)]
20. Li, Y.; Wang, H.; Wang, C.; Xu, J.; Ma, S.; Ou, J.; Zhang, J.; Li, G.; Wei, Y.; Ye, M. Atomically precise structure determination of porous organic cage from Ab initio PXRD structure analysis: Its molecular click postfunctionalization and CO<sub>2</sub> capture application. *ACS Appl. Mater. Interfaces* **2020**, *12*, 17815–17823. [[CrossRef](#)]
21. Hao, G.P.; Li, W.C.; Qian, D.; Lu, A.H. Rapid synthesis of nitrogen-doped porous carbon monolith for CO<sub>2</sub> capture. *Adv. Mater.* **2010**, *22*, 853–857. [[CrossRef](#)] [[PubMed](#)]
22. Zeng, Y.; Zou, R.; Zhao, Y. Covalent organic frameworks for CO<sub>2</sub> capture. *Adv. Mater.* **2016**, *28*, 2855–2873. [[CrossRef](#)] [[PubMed](#)]
23. Ciulla, M.; Canale, V.; Wolicki, R.D.; Pilato, S.; Bruni, P.; Ferrari, S.; Siani, G.; Fontana, A.; Di Profio, P. Enhanced CO<sub>2</sub> capture by sorption on electrospun poly (methyl methacrylate). *Separations* **2023**, *10*, 505. [[CrossRef](#)]
24. Liu, F.; Zhang, Y.; Wang, S.; Gong, T.; Hua, M.; Qian, J.; Pan, B. Metal-free biomass with abundant carbonyl groups as efficient catalyst for the activation of peroxymonosulfate and degradation of sulfamethoxazole. *Chem. Eng. J.* **2022**, *430*, 132767. [[CrossRef](#)]
25. Liebl, M.R.; Senker, J. Microporous functionalized triazine-based polyimides with high CO<sub>2</sub> capture capacity. *Chem. Mater.* **2013**, *25*, 970–980. [[CrossRef](#)]
26. Ashourirad, B.; Sekizkardes, A.K.; Altarawneh, S.; El-Kaderi, H.M. Exceptional gas adsorption properties by nitrogen-doped porous carbons derived from benzimidazole-linked polymers. *Chem. Mater.* **2015**, *27*, 1349–1358. [[CrossRef](#)]
27. Ben, T.; Ren, H.; Ma, S.; Cao, D.; Lan, J.; Jing, X.; Wang, W.; Xu, J.; Deng, F.; Simmons, J.M.; et al. Targeted synthesis of a porous aromatic framework with high stability and exceptionally high surface area. *Angew. Chem. Int. Ed.* **2009**, *48*, 9457–9460. [[CrossRef](#)]
28. Li, G.; Zhang, B.; Yan, J.; Wang, Z. Micro- and mesoporous poly(Schiff-base)s constructed from different building blocks and their adsorption behaviors towards organic vapors and CO<sub>2</sub> gas. *J. Mater. Chem. A* **2014**, *2*, 18881–18888. [[CrossRef](#)]
29. Zhang, H.; Yang, L.M.; Ganz, E. Adsorption properties and microscopic mechanism of CO<sub>2</sub> capture in 1,1-Dimethyl-1,2-ethylenediamine-grafted metal-organic frameworks. *ACS Appl. Mater. Interfaces* **2020**, *12*, 18533–18540. [[CrossRef](#)]

30. Jiang, Y.; Tan, P.; Qi, S.C.; Liu, X.Q.; Yan, J.H.; Fan, F.; Sun, L.B. Metal-organic frameworks with target-specific active sites switched by photoresponsive motifs: Efficient adsorbents for tailorable CO<sub>2</sub> capture. *Angew. Chem. Int. Ed.* **2019**, *58*, 6600–6604. [[CrossRef](#)]
31. Rozaini, M.T.; Grekov, D.I.; Bustam, M.A.; Pré, P. Shaping of HKUST-1 via extrusion for the separation of CO<sub>2</sub>/CH<sub>4</sub> in biogas. *Separations* **2023**, *10*, 487. [[CrossRef](#)]
32. Wahono, S.K.; Stalin, J.; Addai-Mensah, J.; Skinner, W.; Vinu, A.; Vasilev, K. Physico-chemical modification of natural mordenite-clinoptilolite zeolites and their enhanced CO<sub>2</sub> adsorption capacity. *Microporous Mesoporous Mater.* **2020**, *294*, 109871–109880. [[CrossRef](#)]
33. Dabbawala, A.A.; Ismail, I.; Vaithilingam, B.V.; Polychronopoulou, K.; Singaravel, G.; Morin, S.; Berthod, M.; Al Wahedi, Y. Synthesis of hierarchical porous Zeolite-Y for enhanced CO<sub>2</sub> capture. *Microporous Mesoporous Mater.* **2020**, *303*, 110261–110272. [[CrossRef](#)]
34. He, X.; Chen, D.R.; Wang, W.N. Bimetallic metal-organic frameworks (MOFs) synthesized using the spray method for tunable CO<sub>2</sub> adsorption. *Chem. Eng. J.* **2020**, *382*, 122825–122836. [[CrossRef](#)]
35. Niu, J.; Li, H.; Tao, L.; Fan, Q.; Liu, W.; Tan, M.C. Defect engineering of low-coordinated metal-organic frameworks (MOFs) for improved CO<sub>2</sub> access and capture. *ACS Appl. Mater. Interfaces* **2023**, *15*, 31664–31674. [[CrossRef](#)] [[PubMed](#)]
36. Zhai, L.; Huang, N.; Xu, H.; Chen, Q.; Jiang, D. A backbone design principle for covalent organic frameworks: The impact of weakly interacting units on CO<sub>2</sub> adsorption. *Chem. Commun.* **2017**, *53*, 4242–4245. [[CrossRef](#)] [[PubMed](#)]
37. Cui, P.; Jing, X.F.; Yuan, Y.; Zhu, G.S. Synthesis of porous aromatic framework with Friedel-Crafts alkylation reaction for CO<sub>2</sub> separation. *Chin. Chem. Lett.* **2016**, *27*, 1479–1484. [[CrossRef](#)]
38. Xu, S.; He, J.; Jin, S.; Tan, B. Heteroatom-rich porous organic polymers constructed by benzoxazine linkage with high carbon dioxide adsorption affinity. *J. Colloid Interface Sci.* **2018**, *509*, 457–462. [[CrossRef](#)]
39. Wang, X.; Chen, M.; Du, M. A clear insight into the distinguishing CO<sub>2</sub> capture by two isostructural Dy(III)-carboxylate coordination frameworks. *Inorg. Chem.* **2016**, *55*, 6352–6354. [[CrossRef](#)]
40. Li, Z.; Gao, W.; Meng, A.; Geng, Z.; Gao, L. Large-scale synthesis and raman and photoluminescence properties of single crystalline  $\beta$ -sic nanowires periodically wrapped by amorphous SiO<sub>2</sub> nanospheres 2. *J. Phys. Chem. C* **2009**, *113*, 91–96. [[CrossRef](#)]
41. Zhong, B.; Kong, L.; Zhang, B.; Yu, Y.; Xia, L. Fabrication of novel hydrophobic SiC/SiO<sub>2</sub> bead-string like core-shell nanochains via a facile catalyst/template-free thermal chemical vapor deposition process. *Mater. Chem. Phys.* **2018**, *217*, 111–116. [[CrossRef](#)]
42. Buyukcakir, O.; Seo, Y.; Coskun, A. Thinking outside the cage: Controlling the extrinsic porosity and gas uptake properties of shape-persistent molecular cages in nanoporous polymers. *Chem. Mater.* **2015**, *27*, 4149–4155. [[CrossRef](#)]
43. Tian, Y.; Zhu, G. Porous aromatic frameworks (PAFs). *Chem. Rev.* **2020**, *120*, 8934–8986. [[CrossRef](#)] [[PubMed](#)]
44. Yang, Z.; Chen, H.; Wang, S.; Guo, W.; Wang, T.; Suo, X.; Jiang, D.E.; Zhu, X.; Popovs, I.; Dai, S. Transformation strategy for highly crystalline covalent triazine frameworks: From staggered AB to eclipsed AA stacking. *J. Am. Chem. Soc.* **2020**, *142*, 6856–6860. [[CrossRef](#)] [[PubMed](#)]
45. Zhang, Z.; Sun, N.; Wei, W. Facile and controllable synthesis of ordered mesoporous carbons with tunable single-crystal morphology for CO<sub>2</sub> capture. *Carbon* **2020**, *161*, 629–638. [[CrossRef](#)]
46. Shi, X.; Xiao, H.; Azarabadi, H.; Song, J.; Wu, X.; Chen, X.; Lackner, K.S. Sorbents for the direct capture of CO<sub>2</sub> from ambient air. *Angew. Chem. Int. Ed.* **2020**, *59*, 6984–7006. [[CrossRef](#)]
47. Saning, A.; Dubadi, R.; Chuenchom, L.; Dechtrirat, D.; Jaroniec, M. Microporous carbons obtained via solvent-free mechanochemical processing, carbonization and activation with potassium citrate and zinc chloride for CO<sub>2</sub> adsorption. *Separations* **2023**, *10*, 304. [[CrossRef](#)]
48. Karka, S.; Kodukula, S.; Nandury, S.V.; Pal, U. Polyethylenimine-modified zeolite 13X for CO<sub>2</sub> capture: Adsorption and kinetic studies. *ACS Omega* **2019**, *4*, 16441–16449. [[CrossRef](#)]
49. Qiao, Y.; Zhan, Z.; Yang, Y.; Liu, M.; Huang, Q.; Tan, B.; Ke, X.; Wu, C. Amine or azo functionalized hypercrosslinked polymers for highly efficient CO<sub>2</sub> capture and selective CO<sub>2</sub> capture. *Mater. Today Commun.* **2021**, *27*, 102338. [[CrossRef](#)]
50. Qi, S.C.; Liu, Y.; Peng, A.Z.; Xue, D.M.; Liu, X.; Liu, X.Q.; Sun, L.B. Fabrication of porous carbons from mesitylene for highly efficient CO<sub>2</sub> capture: A rational choice improving the carbon loop. *Chem. Eng. J.* **2019**, *361*, 945–952. [[CrossRef](#)]
51. Politakos, N.; Barbarin, I.; Cantador, L.S.; Cecilia, J.A.; Mehravar, E.; Tomovska, R. Graphene-based monolithic nanostructures for CO<sub>2</sub> capture. *Ind. Eng. Chem. Res.* **2020**, *59*, 8612–8621. [[CrossRef](#)]
52. Vieira, R.B.; Moura, P.A.S.; Vilarrasa-García, E.; Azevedo, D.C.S.; Pastore, H.O. Polyamine-grafted magadiite: High CO<sub>2</sub> selectivity at capture from CO<sub>2</sub>/N<sub>2</sub> and CO<sub>2</sub>/CH<sub>4</sub> mixtures. *J. CO<sub>2</sub> Util.* **2018**, *23*, 29–41. [[CrossRef](#)]
53. Liu, S.; Jin, Y.; Bae, J.-S.; Chen, Z.; Dong, P.; Zhao, S.; Li, R. CO<sub>2</sub> derived nanoporous carbons for carbon capture. *Microporous Mesoporous Mater.* **2020**, *305*, 110356. [[CrossRef](#)]
54. Zhang, Z.; Wang, K.; Atkinson, J.D.; Yan, X.; Li, X.; Rood, M.J.; Yan, Z. Sustainable and hierarchical porous enteromorpha prolifera based carbon for CO<sub>2</sub> capture. *J. Hazard. Mater.* **2012**, *229–230*, 183–191. [[CrossRef](#)] [[PubMed](#)]
55. Sheng, M.; Dong, S.; Qiao, Z.; Li, Q.; Wang, Z. Large-scale preparation of multilayer composite membranes for post-combustion CO<sub>2</sub> capture. *J. Membr. Sci.* **2021**, *636*, 119595. [[CrossRef](#)]
56. Xu, S.; Huang, H.; Guo, X.; Qiao, Z.; Zhong, C. Highly selective gas transport channels in mixed matrix membranes fabricated by using water-stable Cu-BTC. *Sep. Purif. Technol.* **2021**, *257*, 117979. [[CrossRef](#)]

57. Dhoke, C.; Zaabout, A.; Cloete, S.; Amini, S. Review on reactor configurations for adsorption-based CO<sub>2</sub> capture. *Ind. Eng. Chem. Res.* **2021**, *60*, 3779–3798. [[CrossRef](#)]
58. Raganati, F.; Miccio, F.; Ammendola, P. Adsorption of carbon dioxide for post-combustion capture: A review. *Energy Fuels* **2021**, *35*, 12845–12868. [[CrossRef](#)]

**Disclaimer/Publisher’s Note:** The statements, opinions and data contained in all publications are solely those of the individual author(s) and contributor(s) and not of MDPI and/or the editor(s). MDPI and/or the editor(s) disclaim responsibility for any injury to people or property resulting from any ideas, methods, instructions or products referred to in the content.